metals

MDPI

Article

Predictive Modeling of Thermally Assisted Machining and Simulation Based on RSM after WAAM

Hongyu Tian [1,2,*], Zhenyang Lu [1,2] and Shujun Chen [1]

[1] Welding Research Institute and Engineering Research Center of Advanced Manufacturing Technology for Automotive Components-Ministry of Education, Beijing University of Technology, Beijing 100124, China; lzy@bjut.edu.cn (Z.L.); sjchen@bjut.edu.cn (S.C.)
[2] College of Robotics, Beijing Union University, Beijing 100101, China
* Correspondence: jdthongyu@buu.edu.cn

Abstract: The WAAM (Wire Arc Additive Manufacturing) process is well-respected because of its low cost and high deposition efficiency; nevertheless, the process has the limitations of high heat input and low forming accuracy. Hybrid manufacturing processes employing both additive and subtractive processes can effectively reduce shape error. The predictive modeling of surface roughness in thermally assisted machining is described in this paper on the basis of three important parameters: feed per tooth, spindle speed, and workpiece temperature. The predictive model indicates that temperature has a very significant influence on the surface quality. An experimental study on thermally assisted machining was performed to obtain the variation law of cutting surface quality with temperature in order to determine the optimal process interval of subtractive processes. Through finite element simulation of thermally assisted machining, the influence law of external main cutting force and the internal mean stress of the cutting material were determined.

Keywords: WAAM; surface roughness predictive; thermally assisted milling; response surface methodology; FE simulation

check for updates

Citation: Tian, H.; Lu, Z.; Chen, S. Predictive Modeling of Thermally Assisted Machining and Simulation Based on RSM after WAAM. *Metals* **2022**, *12*, 691. https://doi.org/10.3390/met12040691

Academic Editors: Zhifeng Liu and Congbin Yang

Received: 21 March 2022
Accepted: 13 April 2022
Published: 18 April 2022

1. Introduction

The continually increasing requirements of sustainability, environmental friendliness, and low cost are a basic feature of modern industry, while conventional manufacturing processes often only pursue high rates of manufacturing. Additive Manufacturing (AM) is a technology of near net-shape components in a layer-by-layer fashion. Due to high deposition rates and low-cost equipment, wire and arc additive manufacturing using welding technology provides outstanding advantages for many light metal alloys, such as aluminum alloy, titanium alloy and nickel alloy, etc.

The classification of heat sources for melting metals include gas tungsten arc welding (GTAW) [1], plasma arc welding (PAW), and gas metal arc welding (GMAW), and these can be used in the wire arc additive manufacturing (WAAM) process [2]. Fabricating 3D metallic models of parts with WAAM, it is possible to obtain higher density and improved bonding strength. Nevertheless, no matter what feedback and energy sources are adopted, geometric accuracy and surface quality at the same level as traditional machining processes are still difficult to obtain because of the liquidity of molten metal and the stair-stepping effect of 3D models [3].

A hybrid of additive manufacturing and subtractive processes has been proposed to provide a fundamental solution for overcoming most of these disadvantages [4]. Various hybrid manufacturing techniques have been developed in recent years, such as layered hybrid manufacturing [5], the welding hybrid milling process [6], etc. For the fabrication of complex structural parts, additive manufacturing uses the same discretization and accumulation mechanism [7]. The introduction of subtractive manufacturing can eliminate stacking defects, remove the oxide layer, correct the contour error, and make up for the inherent defects of additive manufacturing to a great extent, with the advantages of the two processes complementing each other, thus expanding the application scope of additive manufacturing [8]. The WAAM process is able to directly accumulate large-sized structural parts in an open environment with high efficiency and low cost, and is unmatched by other additive manufacturing technologies, while milling and material subtraction can effectively be used to solve the problems of low forming accuracy and poor surface quality [9]. This hybrid manufacturing process has unique advantages for the integrated manufacturing of lightweight and large-scale integral wall panel structures, such as those widely used in aerospace and other fields. This process can improve material utilization from 10~20% to more than 90%, thus greatly improving efficiency and reducing the cost. Therefore, this process has broad application prospects against the backdrop of the vigorous advocation of resource conservation and manufacturing efficiency [10].

Rather than aspects of traditional machining processes, such as surface contour, the clamping type of the parts, and their internal performance, in this paper, the use of subtractive manufacturing processes after additive manufacturing will be studied and discussed. To obtain appropriate mechanical properties and sound geometric accuracy, the subtractive process is carried out when the part is still under the residual heat from the additive manufacturing process. This is an important way of saving energy, reducing consumption, improving product efficiency, and achieving sustainable development. Some research about thermally enhanced machining has used external heat sources to heat and soften the workpiece locally in front of the cutting tool [11]. The yield strength and work hardening of the workpiece decrease with increasing temperature in the shear zone. Therefore, plastic deformation makes hard-to-machine materials easier to work with during machining [12]. Finding the optimum process parameters is an important means for improving the feasibility of the thermal machining of aluminum alloy 2219. Determining those parameters by conducting a large number of trial-and-error experiments remains costly, and is a time-consuming process. The use of the response surface methodology (RSM) can prevent this problem and create models that are able to sufficiently forecast the relation between the input parameters and the output [13].

The main purpose of this paper is to obtain the variation law of cutting surface quality with the thermally assisted machining of aluminum alloy on the basis of experiments, so as to gain a reasonable processing range that can be used to direct practical WAAM hybrid subtractive cutting. The prediction of the surface roughness model of the workpiece is based on RSM, by finding the three factors (workpiece temperature, feed per tooth, and spindle speed) that are most capable of affecting the surface quality of the workpiece during the WAAM and milling processes. The influence of these three factors on the surface quality is investigated on the basis of this surface roughness model, while it is also found that the workpiece temperature has a significant influence on the surface quality. The experimental results prove the validity of the model and the feasibility of thermally assisted milling. The reasonable selection of the best processing interval can result in a perfect effect being obtained. In order to obtain the optimal temperature interval, finite element simulations are performed to study the sensitivity of surface quality to temperature. The mechanical properties of the finite element model explain this phenomenon, and the simulation results further verify the validity of the experimental analysis.

2. Materials and Methods

2.1. Materials and System

The chemical composition of the 2219 aluminum alloy used in this paper is shown in Table 1. A plate of 2219 aluminum alloy with a thickness of 10 mm was machined for this experiment with dimensions of 380 mm × 320 mm × 10 mm.

Table 1. Chemical composition of 2219 aluminum alloy (wt.%).

Cu	Mn	Fe	Si	Zr	Zn	V	Ti	Mg	Others	Al
5.8–6.8	0.2–0.4	≤0.3	≤0.2	0.1–0.25	≤0.1	0.05–0.15	0.02–0.1	≤0.02	≤0.15	Bal.

Figure 1 shows a two-robot cooperative experimental system. The welding robot with the torch is equipped with Tandem GMAW power source to implement WAAM, and is an RTI 2000 (IGM Roboter systeme AG, Wiener Neudorf, Austria). In addition, the other robot-mounted milling tool is KR500 (KUKA AG, Augsburg, Bavaria, Germany). The milling robot is equipped with a high-speed electric spindle ES779 (Siemens, Munich, Germany) (maximum spindle speed is 22,000 rpm) [14]. The standard cutting tool was a 3-flute solid carbide flat-end mill with a helix angle of 60° and a diameter of 10 mm.

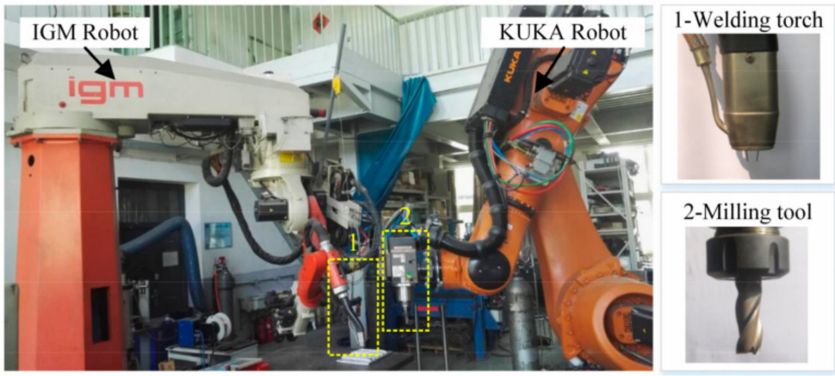

Figure 1. Two-robot cooperative hybrid manufacturing platform.

To simulate the thermally assisted machining environment of the plate workpiece, a heating system was mounted onto the positioner robot, as displayed in Figure 2. Using the TR200 Surface Roughness Tester (Cvok, Shanghai, China), the average surface roughness of the workpiece was determined in order to perform the individual designed tests under different conditions.

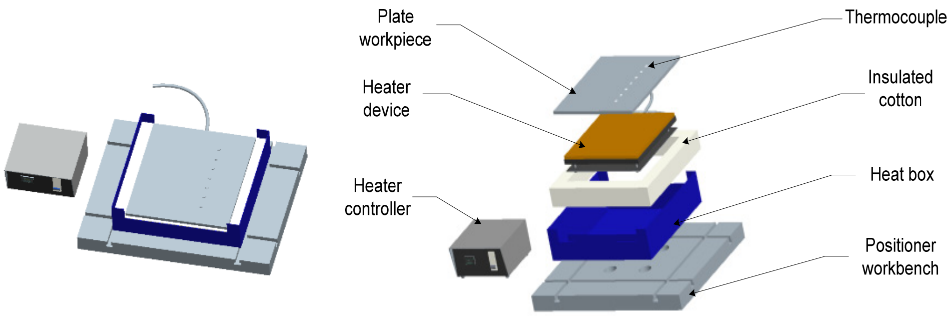

Figure 2. Exploded view of heating system for thermal machining.

2.2. Experimental Design for Thermally Assisted Milling

The machining parameters taken into account during machining in the final milling process are spindle speed, feed rate, and workpiece temperature. These three dependent variables are investigated using RSM. The responses are two surface roughness parameters *Ra* and *Rz* (surface point height of irregularities). The arithmetic mean height (*Ra*), which is also known as the center line average surface roughness, is the arithmetical mean deviation of the vertical coordinates throughout the assessment profile. The maximum height of the profile (*Rz*), named peak–valley surface roughness, is defined as the vertical distance between the highest peak and the lowest valley within the assessment length, which indicates that *Rz* is sensitive to high peaks and low scratches.

The Central Composite Design (CCD) for RSM was coded with five levels: $-\alpha$, -1, 0, +1, $+\alpha$ [15]. To improve prediction accuracy, a rotatable design was used, while the value of α was 1.682. Twenty experiments were designed with these five levels and three factors for the estimation of the pure error sum of squares under the central conditions. The selected cutting parameters were feed per tooth, spindle speed, and workpiece temperature. Table 2 presents the process variables and their ranges. There are 20 rows and 3 columns for the five levels presenting the conditions of the experimental tests. The designed experimental runs and the predicted values of all responses are presented in Table 3, including actual as well as predicted values. Feed per tooth (f_z) is presented in the first column, while the second column presents spindle speed (n), and workpiece temperature (*Temp.*) is allotted the third column, while their interactions are presented in the remaining columns.

Table 2. Table of process variables and their bounds.

Process Variables	Name	Units	Low	High	$-alpha$	$+alpha$
Factor A	f_z	mm/s	0.018	0.042	0.01	0.05
Factor B	n	r/min	1006.75	2493.25	500	3000
Factor C	*Temp.*	°C	110.8	289.2	50	350
Response 1	*Ra*	µm	1.57	2.54	-	-
Response 2	*Rz*	µm	3.21	27.4	-	-

Table 3. Table of CCD with observed and predicted responses.

Std.	Run	f_z	n	*Temp.*	*Ra*	*Rz*
1	6	1.2	1006.8	110.8	2.014	10.287
2	3	1.8	1006.8	110.8	1.768	11.223
3	20	1.2	2493.3	110.8	1.05	5.942
4	13	1.8	2493.3	110.8	0.938	4.93
5	8	1.2	1006.8	289.2	1.255	6.885
6	11	1.8	1006.8	289.2	2.017	13.422
7	18	1.2	2493.3	289.2	0.569	3.207
8	14	1.8	2493.3	289.2	1.51	27.401
9	4	1	1750	200	0.969	5.131
10	7	2	1750	200	1.217	6.711
11	16	1.5	500	200	2.54	14.414
12	15	1.5	3000	200	1.371	9.651
13	12	1.5	1750	50	1.248	7.878
14	1	1.5	1750	350	1.192	6.664
15	10	1.5	1750	200	1.287	7.246
16	17	1.5	1750	200	2.133	10.258
17	19	1.5	1750	200	2.371	13.401
18	2	1.5	1750	200	1.974	10.348
19	9	1.5	1750	200	1.818	10.759
20	5	1.5	1750	200	2.074	10.545

2.3. Development of Surface Roughness Model

The experimental results of surface roughness were analyzed using analysis of variance (ANOVA) to determine the parameters significantly influencing the surface roughness, and the analysis was performed using the Design Expert software package (Design Expert 8.0.7, 2010, Stat-Ease Inc., Minneapolis, MN, USA). The analysis was performed employing a significance level alpha (α) of 0.05 (95% confidence level). The analysis of variance values are presented in Table 4. The model F-value of 5.23 implies that the model is significant. There is only a 0.82% chance that a "Model F-value" this large could occur due to noise. The "Lack of Fit F-value" of 0.17 implies the Lack of Fit is not significant related to pure error. There is a 96.21% chance that a "Lack of Fit F-value" this large could occur due to noise. The fit model is required due to the non-significant Lack of Fit.

Table 4. Analysis of variance table for *R*a.

Source	Sum of Squares	df	Mean Square	F-Value	*p*-Value
Model	4.29	9	0.48	5.23	0.0082 Significant
A-feed	1.04	1	1.04	11.46	0.0069
B-speed	1.45	1	1.45	15.92	0.0026
C-Temp.	0.075	1	0.075	0.82	0.3855
AB	0.083	1	0.083	0.91	0.3634
AC	0.30	1	0.30	3.34	0.0977
BC	1.278×10^{-3}	1	1.278×10^{-3}	0.014	0.9081
A^2	0.36	1	0.36	3.95	0.0749
B^2	2.164×10^{-3}	1	2.164×10^{-3}	0.024	0.8806
C^2	1.07	1	1.07	11.72	0.0065
Residual	0.91	10	0.091	-	-
Lack of fit	0.13	5	0.027	0.17	0.9621 Not significant
Pure error	0.78	5	0.16	-	-
Cor total	5.20	19	-	-	-

The cutting process was optimized on the basis of the BBD (Box-Benhnken Design) developed in the RSM tool of the Design Expert software package. The average surface roughness *R*a was checked on the basis of the values of coefficient of regression (R^2), adjusted R^2, predicted R^2, coefficient of variation (C.V.), predicted residual error sum of squares (PRESS), F-value, and *p*-values (shown in Table 5).

Table 5. Results of variance analysis of *R*a.

Std. Dev.	Mean	C.V.%	PRESS	R-Squared	Adj R-Squared	Pred R-Squared	Adeq Precision
0.30	1.63	18.50	2.17	0.8247	0.6669	0.5820	8.979

The coefficient of regression (R^2) is an important parameter for checking the adequacy of a model. According to Joglekar and May [16], the value of R^2 should be at least 0.80 for the good fitting of a model. In the present study, the value of R^2 for *R*a was 0.8247, which is above this level, showing the adequacy of the model. High values of adjusted R^2 show that the model terms are highly significant. The values of predicted R^2 are the values predicted by the design, which measures the variance in the data predicted by the model. Adequacy of precision measures the signal-to-noise ratio, where ratios greater than 4 are desirable [17,18]. In the present study, the "Pred R-Squared" of 0.5820 is in reasonable agreement with the "Adj R-Squared" of 0.6669. The experimental ratio of 8.979 indicates an adequate signal, as it is higher than 4. PRESS measures the fitting quality of the model at each point in the design. The PRESS value is the sum of the squared differences between the estimated and actual values over all points. A good model will have a low PRESS value [19]. In this study, the PRESS value was 2.17, which is not a high PRESS value, thus indicating the good fitting quality of the model. The C.V. value expresses the variation between actual values and those predicted by the model. The C.V. value of 18.50% in this study is acceptable. According to the values described above, this model can be used to navigate the design space.

In current study, the relationship between the inputs, named X (feed, speed, and temperature of the workpiece), and the outputs, named Y, defines the machinability of AA 2219 in terms of surface roughness. This relationship is given by Equation (1):

$$Y = f(f, n, T) + e_{ij} \tag{1}$$

where Y is the desired machinability aspect and f_z is a function proposed by using a non-linear quadratic mathematical model, which is suitable for studying the interaction effects of process parameters on machinability characteristics. Performing comparisons using ANOVA requires several assumptions to be satisfied. The assumptions underlying the analysis of variance mean that the residuals can be determined using Equation (2):

$$e_{ij} = y_{ij} - \hat{y}_{ij} \tag{2}$$

where e_{ij} is the residual, y_{ij} is the corresponding observation of the runs, and $\hat{y}_{ij}$ is the fitted value [20]. The normality assumption is checked by constructing the normal probability plot of the residuals, as shown in Figure 3. It was concluded that the normality assumption was valid. The other two assumptions were shown to be valid by means of a plot of the residuals versus the fitted values, as illustrated in Figure 4. The structureless distribution of dots above and below the abscissa (the fitted values) shows that the errors were independently distributed, and the variance was constant [21].

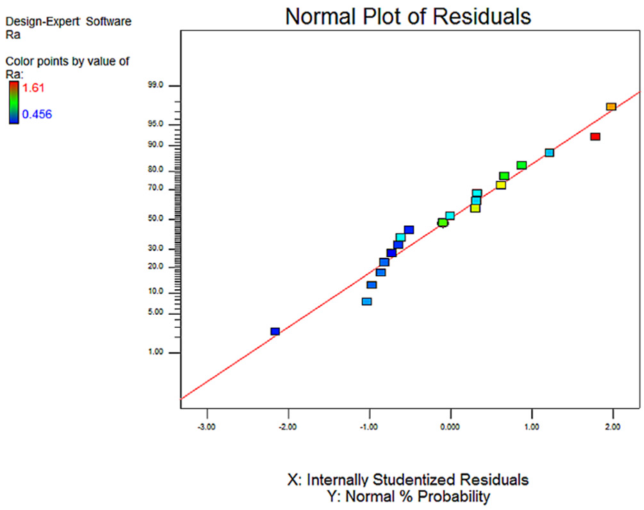

Figure 3. Normal plot of residuals for *R*a.

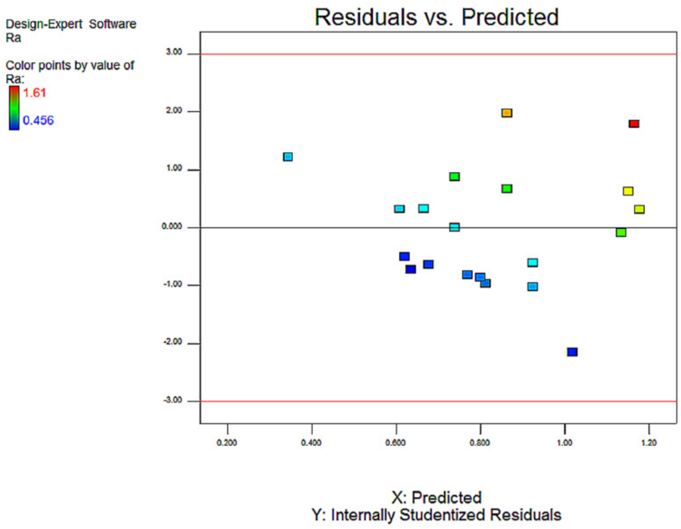

Figure 4. Plot of residuals vs. fitted values for *R*a.

In the present work, the relation between all responses and the operating variables is presented as a second-order mathematical model, as shown in Equation (3):

$$Y = a_0 + \sum_{i=1}^{3} a_i X_i + \sum_{i=1}^{3} a_{ii} X_i^2 + \sum_{i=1}^{3} a_{ij} X_i X_j \tag{3}$$

where a_0 is constant, a_i, a_{ii} and a_{ij} represent the coefficients of linear, quadratic, and cross-product terms, respectively. X_i denotes the coded variables corresponding to the studied machining parameters [22]. The surface roughness (Ra) model is given below in Equation (4), which is described in terms of actual factors.

$$\begin{aligned} R\mathrm{a} \ &= 1.51 + 32.54 f_z - (7.41 \times 10^{-4})\cdot n + (7.06 \times 10^{-3})\cdot T \\ &+0.01 f_z\cdot n + 0.18 f_z\cdot T + (1.91 \times 10^{-7}) n\cdot T - 1098.0 {f_z}^2 \\ &-(2.22 \times 10^{-8}) n^2 - (3.42 \times 10^{-5}) T^2 \end{aligned} \tag{4}$$

On the basis of the analysis of variance presented in Table 4, some parameters can be observed to not be significant. Equation (4) can be simplified to Equation (5), and the surface roughness Rz can be simplified to Equation (6).

$$R\mathrm{a} = 1.51 + 32.54 f_z - (7.41 \times 10^{-4})\cdot n - (3.42 \times 10^{-5})\cdot T^2 \tag{5}$$

$$R\mathrm{z} = 49.34 - 901.63 f_z - 0.015 n - 0.1635 T + 0.22 f_z\cdot n + 3.598 f_z\cdot T \tag{6}$$

3. Results

In the following, the 3D surface plots are considered as a function of two factors at a time. Employing these response factors at fixed levels provides information in the interaction effects with the two input factors, and helps identify the optimum level for each variable in order to achieve the maximum response [23]. Figure 5 shows the surface plot of surface roughness, Ra, when varying the values of feed (A) and speed (B). It can be observed that when increasing spindle speed from 500 to 2493.3 r/min, the roughness value decreases from 2.54 to 0.57 µm. In addition, when increasing feed per tooth from 0.01 to 0.05 mm/min, the roughness value increases from 0.57 to 2.54 µm. The optimal surface roughness can be obtained with a combination of high spindle speed and low feed rate values.

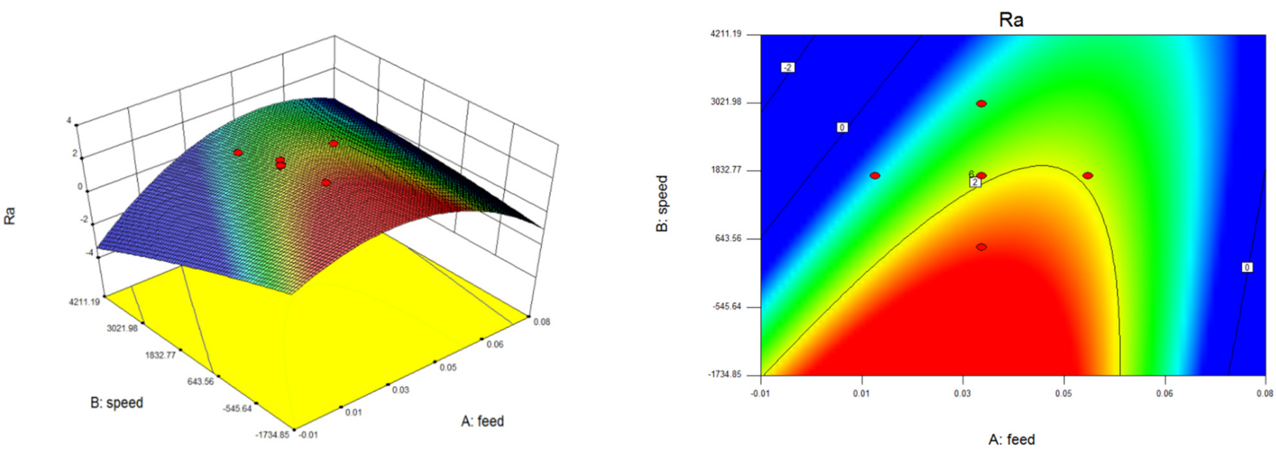

(**a**) (**b**)

Figure 5. 3D surface plot and contour plot of Ra for A and B: (**a**) 3D surface plot; (**b**) contour plot. The red dots in figure indicate the location of the center point in the experimental data distribution graph taken during the experimental design.

Figure 6 shows the surface plot of surface roughness, Ra, when varying the values of feed (A) and temperature (C). It can be observed that with increasing feed rate from 0.02 to 0.03 mm/s, the roughness value decreases, resulting in a better surface quality at high temperature. When increasing the feed rate from 0.03 to 0.05 mm/s, the roughness value first increases and then decreases. The maximum roughness value exceeds 2 µm when the temperature is between 200 and 244.6 °C. The optimal surface roughness can be obtained with a combination of higher temperature, between 244.6 and 289.2 °C, and lower feed rate, between 0.01 and 0.02 mm/s.

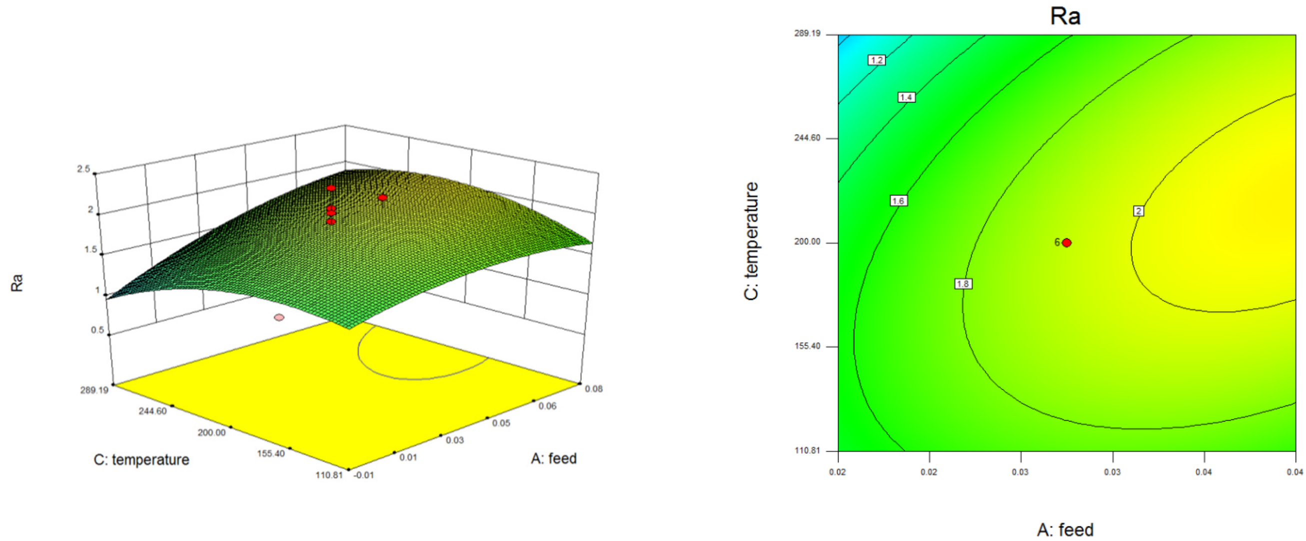

(**a**) (**b**)

Figure 6. 3D surface plot and contour plot of *R*a for A and C: (**a**) 3D surface plot; (**b**) contour plot.

Figure 7 shows the surface plot of surface roughness, *R*a, when varying the values of speed (B) and temperature (C). It can be observed that when increasing the spindle speed from 1898.7 to 2493.3 r/min, the roughness value decreases from 1.4 to 1.8 μm. The surface roughness first increases and then decreases. With increasing spindle speed from 1006.8 to 1898.7 r/min, the roughness value increases from 1.8 to 2.2 μm. When the spindle speed is low, the roughness changes slowly with temperature, on the basis of the contour plot. In addition, the roughness varies rapidly with temperature when the spindle speed is high. The optimal surface roughness can be achieved when using a high spindle speed.

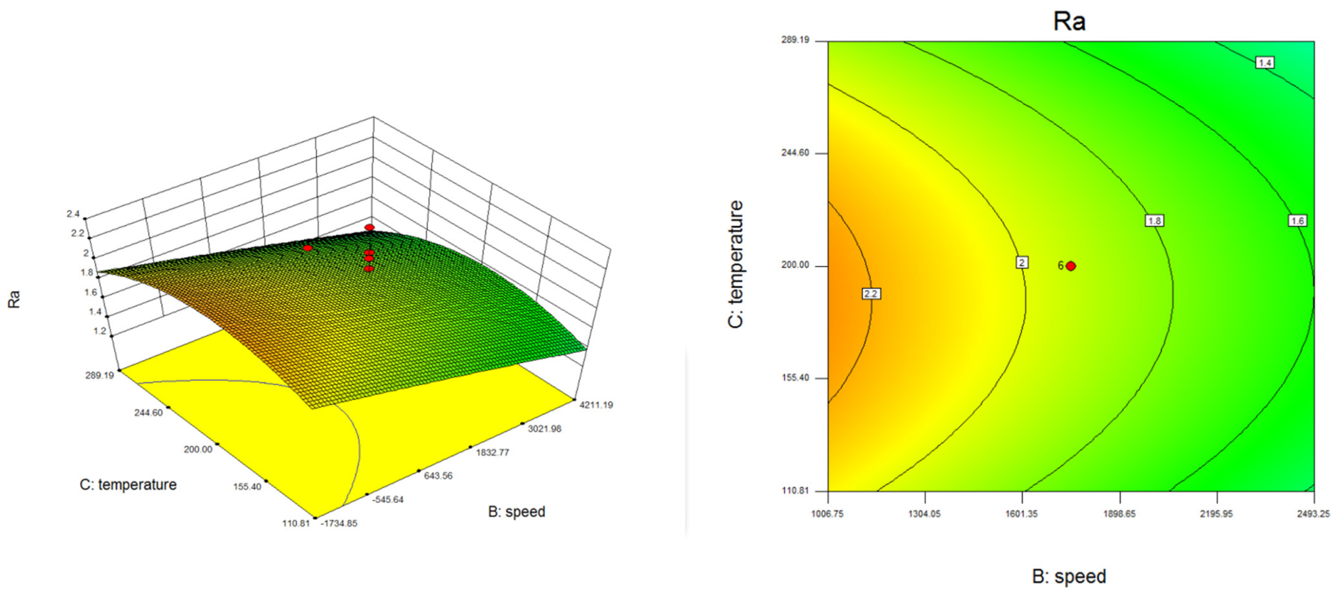

(**a**) (**b**)

Figure 7. 3D surface plot and contour plot of *R*a for B and C: (**a**) 3D surface plot; (**b**) contour plot.

Figure 8 shows the temperature response curve for one of the factors of surface roughness, *R*a. The dashed blue lines in the figure are the predicted upper and lower bounds. The black line represents the predicted temperature curve. The mean surface roughness is 1.404 µm at temperatures between 50 and 110.8 °C and a semi-finished machining level was able to be achieved. The mean surface roughness is 1.775 µm at 200 °C, achieving a rough machining level. At temperatures between 289.2 and 350 °C, the mean of surface roughness is 1.309 µm, whereby a semi-finished machining level can be achieved. It can be observed that the surface roughness first increases and then decreases with increasing workpiece temperature.

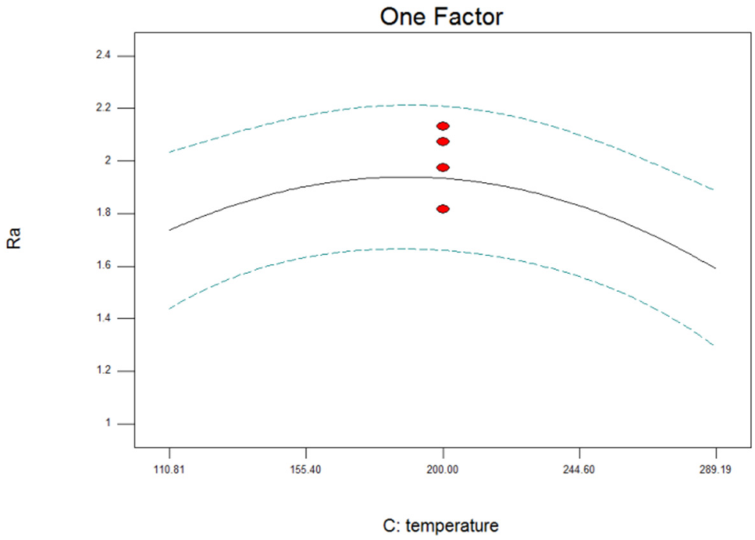

Figure 8. Temperature response curve.

Figure 9 presents the finished workpiece when performing thermally assisted machining at different initial temperatures from 110.8 to 400 °C. Figure 9a–d show the thermal end milling results of the experimental standard sequence 4, 11, 8, 14 using the robot. The cutting depth was 0.2 mm and other parameters were as presented in Table 3. On the basis of the finished workpiece, it is obvious that the chip sticking phenomenon can be clearly observed when the cutting temperature exceeds 200 °C. The cutting tool mark is similar to traditional cutting in the low temperature region (≤200 °C), showing a sharp cross-section state. In addition, because the cutting temperature is close to the solid–liquid phase line in the high-temperature region, the cutting tool mark exhibits a melting wave, as shown Figure 9d. The finished workpiece also indicates that spindle speed has a great influence on the surface quality, see Figure 9b, with low spindle speed (500 r/min) leading to poor surface quality. Comparing Figure 9a,c, it can be observed that the surface quality at lower temperature (110.8 °C) is better than that at higher temperature (298.2 °C) when the feed rate and spindle speed are the same.

Figure 9e presents at the results of attempting high-temperature thermally assisted milling of AA 2219 at 400 °C. The main relevant cutting parameters were: cutting feed per tooth of 0.026 mm/s, spindle speed of 1750 r/min, cutting depth of 0.5 mm, and workpiece temperature of 400 °C. The burr phenomenon can be observed on the side the of the finished workpiece. The maximum burr height is 3.5 mm. The undivided are distributed on both sides of the cutting area in a skirt state. The shape is most similar to the workpiece after friction stir welding, because the material being cut was in a semi-solid state during milling. The high temperature causes the material to enter a semi-solid state, as a result of not only the prefabrication temperature of the workpiece, but also the friction effect of the tool. The surface quality is rather poor when the workpiece temperature is 400 °C. There are no clear tool marks on the surface, but a rough, fish-scale-like surface is evident; obviously, this result was unexpected. In the process of cutting, there is a certain phenomenon of material sticking to the tool, but with the rotation of the tool during the cutting process, the portion of the materials sticking were able to break away from the tool, thus having little effect on the tool.

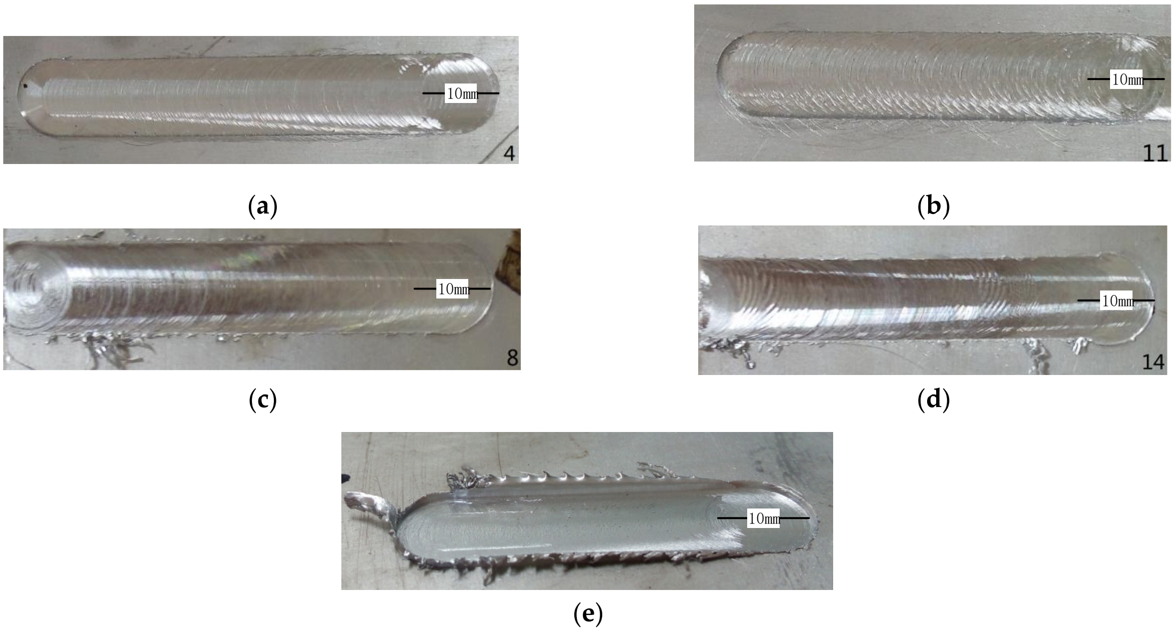

Figure 9. The finished workpiece with different initial temperatures: (**a**) finished workpiece with an initial temperature of 110.8 °C; (**b**) finished workpiece with an initial temperature of 200 °C; (**c**) finished workpiece with an initial temperature of 289.2 °C; (**d**) finished workpiece with an initial temperature of 350 °C; (**e**) finished workpiece with an initial temperature of 400 °C.

The experimental results show that the high-temperature region between 155.4 and 244.6 °C (from Figure 8) is suitable for thermally assisted milling. Temperatures over 300 °C are not an option, as the material is in a semi-solidified state with a partially melted cutting surface, resulting in difficulty in controlling the surface quality.

4. Finite Element Simulation

To research its sensitivity to temperature, the thermally assisted milling process was simulated using ABAQUS/Standard with two-dimensional orthogonal cutting under plane strain conditions. Using this commercial finite element software made it possible to study the effects of accumulated strain and temperature on the final residual stress profile induced by the machining process. The constitutive model of the material is the Johnson–Cook model [24], which has been widely used in metal cutting simulations because it is able to reflect the constitutive behavior of metal under conditions of high strain, high strain rate, and high temperature. Equation (7) shows the model:

$$\sigma = f(\varepsilon) \cdot f(\dot{\varepsilon}) \cdot f(T) = (A + B\varepsilon^n)[1 + C\ln(\frac{\dot{\varepsilon}}{\dot{\varepsilon}_0})][1 - (\frac{T - T_r}{T_m - T_r})^m] \tag{7}$$

The parameter σ is equivalent plastic stress, and ε is equivalent plastic strain. The parameter $\dot{\varepsilon}$ is equivalent plastic strain rate, and $\dot{\varepsilon}_0$ is reference strain rate. The parameters T and T_m are the dynamic temperature and the melting temperature of material, respectively, and T_r is room temperature [25]. The constant A is initial yield stress, B is hardening modulus, C is the strain rate dependence coefficient, n is the work hardening index, and m is the thermal softening coefficient [26]. The five material constants, A, B, C, n and m, were obtained on the basis of tensile tests for aluminum alloy materials, as presented in Table 6. The aluminum alloy matrix was modeled as a thermal-elastic-plastic material, and the material parameters applied in the FE computational analysis are listed in Table 7.

Table 6. Material constants for the Johnson–Cook constitutive equation of 2219 Al and 2A12 Al.

Matrix Material	A/(MPa)	B/(MPa)	C	n	m	T_m/(K)	T_r/(K)
AA 2219	170	228	0.028	0.31	2.75	816	298
AA 2A12	370.4	1798.7	0.0128	0.733	1.528	775	298

Table 7. Material parameters for the analysis.

Material Properties	AA 2219	AA 2A12	YG8 (Cutting Tool)
Density/(kg m^{-3})	2840	2700	-
Modulus of elasticity/(GPa)	70	71.3	650
Poisson's ratio	0.3	0.33	0.25
Coefficient of thermal expansion/($\times 10^{-6}$ K^{-1})	23	23.3	4.9
Thermal conductivity /(W·m^{-1}·K^{-1})	116	130	59
Specific heat capacity /(J·kg^{-1}·K^{-1})	900	921	334

According to the Johnson–Cook model, D is defined as a damage parameter in an element. Chip separation occurs when the following condition (Equation (8)) is satisfied.

$$D = \sum \frac{\Delta \varepsilon}{\varepsilon^f} = 1 \tag{8}$$

Parameter $\Delta\varepsilon$ in Equation (8) is the change in equivalent plastic strain during the integration cycle, and ε^f is the equivalent strain at fracture as a function of temperature, strain rate, equivalent stress, and pressure, as expressed in Equation (9) [27].

$$\varepsilon^f = [d_1 + d_2 \exp(d_3\sigma^*)][1 + d_4 \ln(\frac{\dot{\varepsilon}}{\dot{\varepsilon}_0})][1 + d_5(\frac{T - T_r}{T_m - T_r})] \tag{9}$$

The parameter σ^* is the stress triaxiality, and d_1...d_5 are the failure parameters, which were obtained from previous experimental research and which are listed in Table 8. The FE model of the tool–workpiece pair for the purposes of numerical assessment is shown in Figure 10.

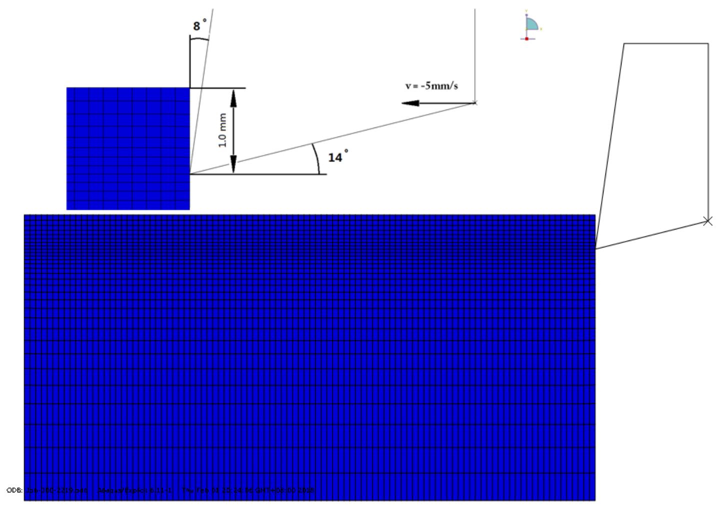

Figure 10. Finite element simulation results of the FE model of the tool–workpiece pair.

Table 8. Failure parameters for the Jonhson-Cook failure criterion of AA 2219 and AA 2A12.

Matrix Material	d_1	d_2	d_3	d_4	d_5
AA 2219	0.13	0.10	−1.5	0.01	0.1
AA 2A12	0.116	0.211	−2.172	0.012	−0.01256

Figure 11 presents the simulation results of Von Mises stress and chip formation at a chip thickness of 1.0 mm chip during thermally assisted milling at a cutting velocity of 5 mm/s and an edge radius of 0.01 mm. It can be observed that the maximum chip stress was located near the tool–chip interface, referred to as the primary shear zone.

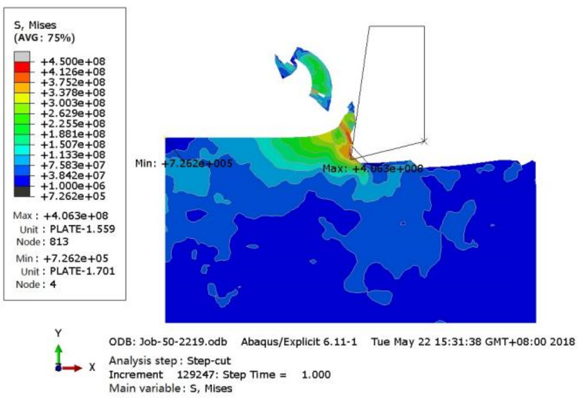

(**a**)

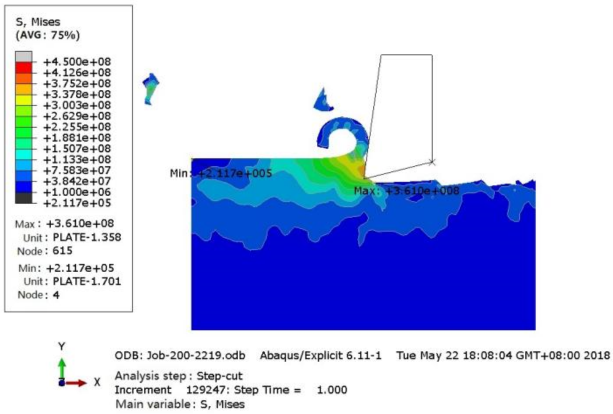

(**b**)

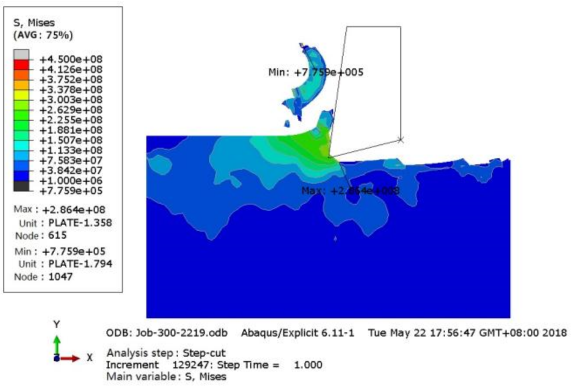

(**c**)

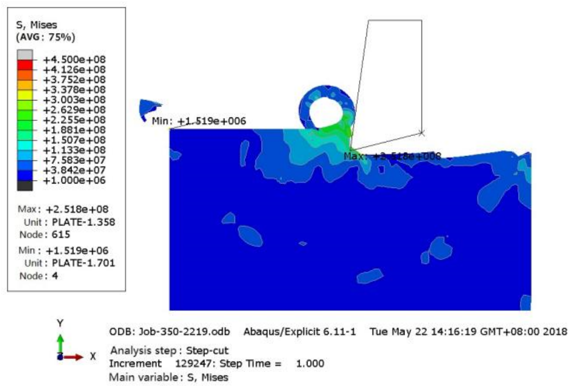

(**d**)

Figure 11. Cloud images for the simulation of Von Mises stress during thermally assisted cutting: (**a**) initial workpiece temperature of 50 °C; (**b**) initial workpiece temperature of 200 °C; (**c**) initial workpiece temperature of 300 °C; (**d**) initial workpiece temperature of 350 °C.

On the basis of the cloud images, the stress distribution area can be observed to be larger at low temperatures, while the stress change becomes concentrated in a small area with increasing workpiece substrate temperature. The maximum stress occurs in the first cutting deformation area, that is, the cutting slip area, at the contact area between the main cutting edge of the tool and the workpiece. Maximum stress decreases with increasing workpiece substrate temperature, as can be observed from the color distribution of the cutting area in the cloud images. It can be seen from the four cloud images that stripping the chips from the workpiece is no more difficult or easy with increasing temperature. Limited by the two-dimensional orthogonal cutting simulation software, there is no material solidification or occurrence of the chip skirt phenomenon during material cutting. Simulations at higher substrate temperatures were attempted, but the software results were distorted.

Figure 12 shows the change curve of maximum Von Mises stress at different initial workpiece temperatures. It can be seen that the stress decreases with increasing initial temperature. The simulated Von Mises stress results indicate that the variation tendency of the mean stress in the workpiece is similar to that found in traditional machining. The mean stress decreases with increasing temperature, especially during the high-temperature stage, thus proving that thermally assisted milling of aluminum alloy 2219 at 200–300 °C is feasible. However, the temperature setting for thermally assisted milling should not be too high due to the solid–liquid transition temperature being 548.2 °C in the binary phase diagram of Al-Cu when matrix prefabrication is performed at a temperature above 240 °C. Previous thermally assisted milling experiments show that when the temperature of workpiece is 400 °C, cutting is not easy due to the softening of the material.

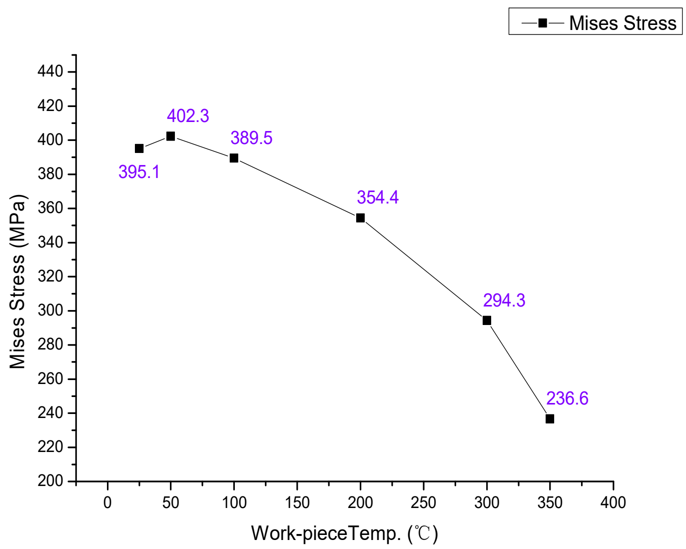

Figure 12. Von Mises stress at different workpiece temperatures.

Figure 13 shows the mean change in reaction force on the cutting tool at different workpiece temperatures. It can be seen that the workpiece suffered higher drag force when the temperature was in the lower region. Thermal cutting resistance is mainly reflected in the forward reaction force of the material to the tool on the *X*-axis. On the basis of the mean reaction force curve, the setting temperature of the workpiece can still be placed in the high-temperature region of 150–300 °C. The required cutting force decreases with increasing temperature, which makes the material easier to cut.

The data analysis of reaction force is presented in Table 9. It can be observed that the mean relative errors of reaction force (*X*-axis direction: tool cutting in the forward direction) are all less than 20%, ranging from 5.59% to 17.97%, thus proving the reliability of the analysis. The mechanical characteristics of the FE model determined on the basis of the simulation results are similar to those determined on the basis of the experimental analysis.

Table 9. Data analysis of reaction force in the *X*-axis direction.

Temperature of Workpiece/(°C)	Mean of *X*-Axis RF /(MPa)	Variance of RF	Mean Relative Error of RF
25	258.3	0.356	13.78%
50	245.1	0.364	14.83%
110	257.3	0.462	17.97%
200	231.9	0.339	14.64%
300	191.6	0.112	5.82%
350	171.5	0.096	5.59%

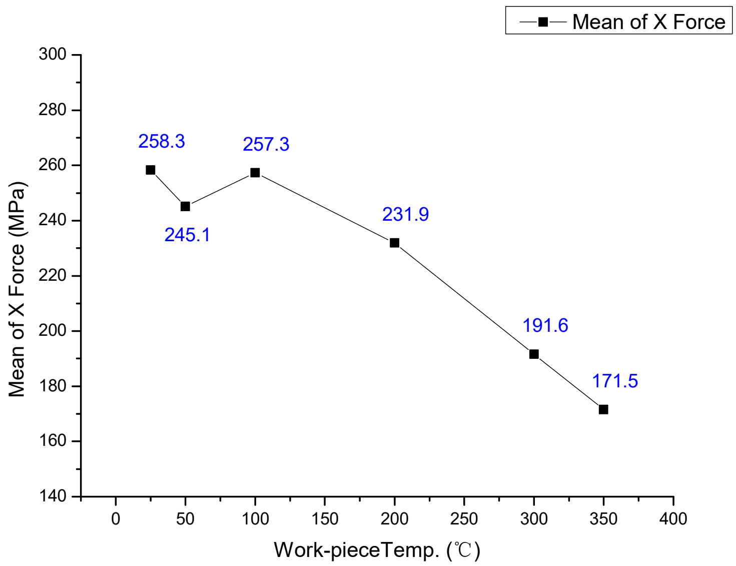

Figure 13. Mean reaction force at different workpiece temperatures.

5. Conclusions and Future Work

The experimental results on thermally assisted machining show that the surface roughness first increases and then decreases with increasing temperature of the workpiece, and that a finished or semi-finished machining level can be achieved.

The optimal process interval of the subtractive process is in the high-temperature region (155.4–244.6 °C) of thermally assisted milling, but the surface roughness *R*a consists of a rising section and a falling section.

On the basis of macro observations of the cutting surface quality, when cutting at high temperatures of over 300 °C, the cutting burr appears to be too large, and chips stick to the tool.

On the basis of FE simulation, the external reaction force of thermal cutting decreases with increasing initial temperature because of the softening of the material.

The internal mean stress of the cutting material decreases with increasing initial temperature. Meanwhile the stress concentration area decreases with increasing initial temperature on the basis of the Von Mises stress cloud.

This paper only provides the variation law of the surface roughness of aluminum alloy 2219 with thermally assisted machining, and the optimum cutting process interval is not given. Through experimental research, the best cut-in point for subtractive processes in hybrid manufacturing can be determined, with the aim of reducing the cooling time of the matrix while waiting for additive manufacturing components and improving machining efficiency. Future work will focus on the mechanism of the internal microstructure change in cutting materials during thermally assisted machining, such as effects of external cutting factors on variations in internal energy and internal strain in materials.

Author Contributions: Conceptualization, Z.L. and S.C.; methodology, H.T.; software, H.T.; validation, Z.L., S.C. and H.T.; formal analysis, H.T.; investigation, Z.L.; resources, S.C.; data curation, H.T.; writing—original draft preparation, H.T.; writing—review and editing, H.T.; visualization, H.T.; supervision, Z.L.; project administration, Z.L.; funding acquisition, S.C. All authors have read and agreed to the published version of the manuscript.

Funding: This work was supported by the National Natural Science Foundation of China under Grants No. 51475008 and No. 51775007.

Institutional Review Board Statement: Not applicable.

Informed Consent Statement: Not applicable.

Data Availability Statement: The data presented in this study are available on request from the corresponding author.

Acknowledgments: The authors would like to thank the lab managers of the Welding Research Institute and Engineering Research Center of Beijing University of Technology for the materials used for the experiments.

Conflicts of Interest: The authors declare no conflict of interest.

References

1. Geng, H.; Li, J. Optimization of wire feed for GTAW based additive manufacturing. *J. Mater. Process. Technol.* **2017**, *243*, 40–47. [CrossRef]
2. Zhang, C.; Li, Y. Wire arc additive manufacturing of Al-6Mg alloy using variable polarity cold metal transfer arc as power source. *Mater. Sci. Eng. A* **2018**, *711*, 415–423. [CrossRef]
3. Kumbhar, N.N.; Mulay, A.V. Post processing methods used to improve surface finish of products which are manufactured by additive manufacturing technologies: A review. *J. Inst. Eng. India Ser. C* **2018**, *99*, 481–487. [CrossRef]
4. Flynn, J.M.; Shokrani, A. Hybrid additive and subtractive machine tools–research and industrial developments. *Int. J. Mach. Tools Manuf.* **2016**, *101*, 79–101. [CrossRef]
5. Tiago, A.R.; Duarte, V.; Miranda, R.M. Current status and perspectives on wire and arc additive manufacturing (WAAM). *Materials* **2019**, *12*, 1121.
6. Lopes, J.G.; Machado, C.M. Effect of milling parameters on HSLA steel parts produced by wire and arc additive manufacturing (WAAM). *J. Manuf. Process.* **2020**, *59*, 739–749. [CrossRef]
7. He, R.; Zhou, N.; Zhang, K.; Zhang, X.; Zhang, L.; Wang, W.; Fang, D. Progress and challenges towards additive manufacturing of SiC ceramic. *J. Adv. Ceram.* **2021**, *10*, 638. [CrossRef]
8. Krner, C.; Markl, M.; Koepf, J.A. Modeling and Simulation of Microstructure Evolution for Additive Manufacturing of Metals: A Critical Review. *Metall. Mater. Trans. A* **2020**, *51*, 4970–4983. [CrossRef]
9. Alimi, O.A.; Meijboom, R. Current and future trends of additive manufacturing for chemistry applications: A review. *J. Mater. Sci.* **2021**, *56*, 16824–16850. [CrossRef]
10. Li, C.; Ferry, M.; Kruzic, J.J.; Li, X. Review: Multi-principal element alloys by additive manufacturing. *J. Mater. Sci.* **2022**, 1–33. [CrossRef]
11. Venkatesh, G.; Chakradhar, D. Influence of thermally assisted machining parameters on the machinability of inconel 718 superalloy. *Silicon* **2017**, *9*, 867–877. [CrossRef]
12. Ganta, V.; Sagar, K.S. Multi objective optimization of thermally enhanced machining parameters of inconel 718 using grey relational analysis. *Int. J. Mach. Mach. Mater.* **2017**, *19*, 57.
13. Lucas, J.M. Response surface methodology: Process and product optimization using designed experiments, 3rd edition. *J. Qual. Technol.* **2017**, *21*, 228–230. [CrossRef]
14. Li, F.; Chen, S. Evaluation and optimization of a hybrid manufacturing process combining wire arc additive manufacturing with milling for the fabrication of stiffened panels. *Appl. Sci.* **2017**, *7*, 1233. [CrossRef]
15. Bajpai, S.; Gupta, S.K. Application of central composite design approach for removal of chromium (VI) from aqueous solution using weakly anionic resin: Modeling, optimization, and study of interactive variables. *J. Hazard. Mater.* **2012**, *227–228*, 436–444. [CrossRef]
16. Joglekar, A.M.; May, A.T. Product excellence through design of experiments. *Cereal Food World* **1987**, *32*, 857–868.
17. Maran, J.P.; Manikandan, S. Response surface modeling and optimization of process parameters for aqueous extraction of pigments from prickly pear (opuntia ficus-indica) fruit. *Dyes Pigments* **2012**, *95*, 465–472. [CrossRef]
18. Maran, J.P.; Manikandan, S. Box-Behnken design based multi-response analysis and optimization of supercritical carbon dioxide extraction of bioactive flavonoid compounds from tea (*Camellia sinensis* L.) leaves. *J. Food Sci. Technol.* **2015**, *51*, 92–104. [CrossRef]
19. Garg, K.K.; Prasad, B. Development of Box Behnken design for treatment of terephthalic acid wastewater by electrocoagulation process: Optimization of process and analysis of sludge. *J. Environ. Chem. Eng.* **2016**, *4*, 178–190. [CrossRef]
20. Hosseini, M.; Ahmadi, S.R. Experimental and finite element analysis of EDM process and investigation of material removal rate by response surface methodology. *Int. J. Adv. Manuf. Technol.* **2013**, *69*, 687–704. [CrossRef]
21. Montgomery, D.C.; Runger, G.C. *Applied Statistics and Probability for Engineers*, 6th ed.; John Wiley & Sons Inc.: New York, NY, USA, 2003.
22. Zahia, H.; Athmane, Y.M. On the application of response surface methodology for predicting and optimizing surface roughness and cutting forces in hard turning by PVD coated insert. *Int. J. Ind. Eng. Comput.* **2015**, *6*, 267–284. [CrossRef]
23. Shaik, J.H.; Srinivas, J. Optimal selection of operating parameters in end milling of Al-6061 work materials using multi-objective approach. *Mech. Adv. Mater. Mod. Process.* **2017**, *3*, 5. [CrossRef]
24. Johnson, G.R.; Cook, W.H. A construetive model and data for metals subjected tolarge strains, high strain rates and high temperatures. In Proceedings of the 7th International Symposium on Ballistics, Hague, The Netherlands, 19–21 April 1983; pp. 541–547.
25. Duan, C.; Sun, W. Modeling and simulation of tool-chip interface friction in cutting Al/SiCp composites based on a three-phase friction model. *Int. J. Mech. Sci.* **2018**, *142–143*, 384–396. [CrossRef]

26. Fan, Y.H.; Wang, T. Surface residual stress in high speed cutting of superalloy Inconel 718 based on multiscale simulation. *J. Manuf. Process.* **2018**, *31*, 480–493. [CrossRef]
27. Zhou, L.; Cui, C. Finite element and experimental analysis of machin-ability during machining of high-volume fraction SiCp/Al composites. *Int. J. Adv. Manuf. Technol.* **2017**, *91*, 1935–1944. [CrossRef]